*Egypt. J. Chem.* **Vol. 67,** No. 6 pp. 233 - 238 (2024)

# Egyptian Journal of Chemistry

**http://ejchem.journals.ekb.eg/**

## MOFs-derived 3D porous $ZnCo_2O_4$ nanocubes intercalated 3D graphene electrode for superior lifespan hybrid supercapacitors

**Ahmed G. El-Deen[a]*, Mariam K. Sohby [b] and Karim Menoufi[a]**

[a]*Renewable Energy Science and Engineering Department, Faculty of Postgraduate Studies for Advanced Sciences (PSAS), Beni-Suef University, Beni-Suef 62511, Egypt.*

[b]*Material science and nanotechnology Department, Faculty of Postgraduate Studies for Advanced Sciences (PSAS), Beni-Suef University, Beni-Suef 62511, Egypt*

**Abstract**

Despite the escalating energy crisis and mounting environmental concerns, it is evident that conventional energy storage can no longer fulfil the demands of modern society. Consequently, supercapacitors have gained significant popularity as energy storage devices owing to their outstanding efficiency. Nevertheless, the limited energy density of this substance restricts its potential applications. Herein, the robust and controllable design of ultra-porous zinc cobaltite nanocubes ($ZnCo_2O_4$ Nc) is successfully fabricated using a MOF-templated approach. The $ZnCo_2O_4$ Nc is interconnected with 3D graphene nanosheets ($ZnCo_2O_4$ Nc@3DGr) as electrodes for hybrid storage devices. However, the ($ZnCo_2O_4$ Nc@3DGr) nanocomposite electrode exhibits better specific capacity/capacitance of (824.4 C/g, 1374 F/g) at a current density of 1 A /g compared to pristine $ZnCo_2O_4$ Nc (567 C/g, 945 F/g). For Full cell device configuration, the designed hybrid supercapacitor (HSC) is constructed using $ZnCo_2O_4$ Nc@3DGr (positive) and 3DGr (negative) electrodes. The constructed $ZnCo_2O_4$ Nc@3DGr //3DGr hybrid device delivers a maximum energy density of 60 Wh/kg with a power density of 800 W/kg and an ultralong lifetime with a minimum ~7% capacitance loss up to 11,000 cycles.

*Keywords*: MOFs-template; bimetallic oxides. Hybrid storage device; ultralong lifespan

### 1. Introduction

The increasing demand for increasingly powerful mobile gadgets and electric vehicles has led to a growing need for superior energy storage technologies with outstanding efficiency capabilities [1,2]. Supercapacitors have considerable potential as an electrochemical energy storage technology due to their many benefits compared to conventional capacitors[3]. These advantages include an extended lifetime, high-power density, cheap cost, high-rate capability, and rapid charging speed [4]. However, limitation of desirable materials-based electrodes that meet the high requirement of high energy poses a critical challenge[5]. Hybrid supercapacitors (HSCs) can address the gap between the excellent energy density of batteries and the exceptional power density of electric double-layer capacitors (EDLCs) [6,7]. The HSC device integrates EDLC based carbon electrodes and battery-type-based materials within a composite including bimetallic oxides, sulphides, or phosphides[8–10]. Limitations in rate and cycle performances due to sluggish reaction kinetics and poor conductivity may prevent battery-type materials from being widely used in the future [11,12]. Compared to conductive polymers or carbonaceous materials, transition metal oxides are preferred because of their superior stability, cheap cost, and abundance of oxygen valence states[13,14]. Metal-organic frameworks (MOFs) have gained prominence in recent years due to their inherent benefits, such as exceptional surface area, structural variety, functionality, and diverse porous structure. These characteristics enable MOFs highly suitable for various purposes in particular energy storage applications. Furthermore, when used as reinforcements and sacrificial templets [15–17]. The incorporation of metal-organic frameworks (MOFs) with diverse functional materials is an extremely beneficial and viable approach for enhancing the performance of MOFs or introducing novel functionalities to facilitate their practical uses furthermore it can be utilized as reinforcements and sacrificial templets for synthesizing different dimensional nanomaterials such as 1D, 2D, 3D Mono/Bi-metallic oxides[18–20].

Among transition metal oxides, spinel-type metal oxides ($AB_2O_4$) gained the most significant interest as an ideal battery-type electrode-based storage device[21,22]. Huge efforts have been devoted to improving the battery-type electrode at high power and energy densities by developing porous nanostructured materials with optimal pore geometry, and short ionic route [23,24]. $ZnCo_2O_4$ is a prominent spinel-type metal oxide because it has a much larger energy storage capacity than other metal oxides [15]. $ZnCo_2O_4$ was synthesized utilizing a variety of techniques, including hydrothermal, sol-gel coprecipitation, and electrodeposition[25–28]. For example, Jai Bhagwan et al. created $ZnCo_2O_4$ nanoparticles via a facile combustion process under various calcination conditions, the calcinated sample at 600 ºC achieved good specific capacitance (Cs) of (843 F/g at 1 A/g)[29]. Xu et al. employed a hydrothermal

*Corresponding author e-mail: ag.eldeen@psas.bsu.edu.eg.; (Ahmed G. El-Deen).

Receive Date: 19 October 2023, Revise Date: 12 November 2023, Accept Date: 23 November 2023

DOI: 10.21608/EJCHEM.2023.243526.8749

technique to design $ZnCo_2O_4$ nanoribbon that showed a remarkable capacitance of (776.2 at 1 A/g) and good revisability rate [30]. Rajesh and colleagues developed microsphere $ZnCo_2O_4$ , which achieved a capacitance performance of (854 F/g at 2 A/g) moreover ~ 8% capacity loss after 3000 cycles [31]. Furthermore, Shang et al. prepared a unique 3D $ZnCo_2O_4$ peony-like structure that delivered a capacitance of ($C_s = 440$ F /g at 1 A/ g)[32]. However, the majority of the resulting 0D, 1D, and 2D structures (nanoparticles, nanorods/nanowires, and nanosheets) exhibit agglomeration, sheet aggregations, and poor interaction area. As a result, using a MOFs-template technique to fabricate a 3D porous $ZnCo_2O_4$ Nc structure may enhance interfacial contact surface area, promote storing charge, and improve ionic channels. To overcome the conductivity constraint of bimetallic oxides, integrating $ZnCo_2O_4$ Nc with conductive polymer or graphene can provide an achievable way to enhance the electrochemical features [33].

This work reports a facile route and unique $ZnCo_2O_4$ nanocubes (Nc) design with a multi-porous 3D structure followed by 3D graphene layers as a hosting net framework structure. We found that the nanocomposite-based electrodes display mixed behaviour of EDLC and battery-type with specific capacity compared with those of pristine $ZnCo_2O_4$. The $ZnCo_2O_4$ Nc@3DGr nanocomposite electrode revealed significant electrochemical efficiency and high-rate capability. The designed HSCs employing 3DGr (negative) and the $ZnCo_2O_4$ Nc@3DGr (positive) deliver a substantial energy density and a long-lasting device that maintains capacitance after 11,000 charge/discharge cycles.

## 2. Experimental section

### *2.1. Chemicals*

Ultrafine graphite flacks 99%, cobalt nitrate hexahydrate (≥98%), Zinc nitrate tetrahydrate (98%), and 2-methylimidazole (99%), all chemicals were purchased from Sigma-Aldrich.

### *2.2. Synthesis of porous $ZnCo_2O_4$ nanocubes*

Initially, a certain amount of 0.5 mmol of Zinc nitrate and 1 mmol of cobalt nitrate were dissolved into 25 mL of DI ($H_2O$). In a subsequent experiment, a solution containing 2-methylimidazole at a concentration of 4 mM was prepared by dissolving it in 20 mL of methanol. Subsequently, the imidazole compound was injected into the mixture aqueous solution with vigorously stirring for 20 min at room temperature. The solution was left undisturbed for a period of about 24 hours to enhance the progress of the chemical reaction. The produced pale purple crystals were collected using a centrifuge, followed by several washes with methanol to eliminate any remaining unreacted organic linkers. Subsequently, the crystals were subjected to a drying process overnight at a temperature of 70 °C inside a vacuum oven to produce the (Zn-Co ZIF) material. For Bimetallic oxide ($ZnCo_2O_4$) conversion, the obtained Zn-Co ZIF was calcinated in the air at 450 °C for 4 hours with a 3 °C per min heating rate.

### *2.3. Synthesis of $ZnCo_2O_4$ Nc@3D porous graphene.*

Graphene oxide (GO) was produced via a modified Hummers process [34]. Typically, 70 mg of the fabricated $ZnCo_2O_4$ dispersed into 150 mL of graphene oxide (GO) distributed in a solution with a 5 mg/mL concentration was combined with 0.5 mL of triethylenetetramine. The resulting mixture was subjected to sonication for a duration of 15 minutes at room temperature. The mixture was introduced into a Teflon tube autoclave with a capacity of 200 mL and exposed to thermal treatment at 160 °C for 24 hours. A sponge-like cake was immersed in 250 mL of deionized water for a duration of 2 hours. Subsequently, it was frozen overnight at a temperature of -20 °C. Following this, the produced hydrogel nanocomposite was subjected to a lyophilized process lasting 48 hours. For pure 3D graphene (3DGr), the same progress is utilized without the addition of $ZnCo_2O_4$ Nc.

### *2.4. Electrode preparation and electrochemical investigation*

A homogeneous slurry was formed by dissolving 90% of the active ingredients in 10 mL Dimethylformamide (DMF) with 10% (binder, PVDF) and mixing for 25 minutes. The slurries were coated on Ni-foam and dried for 12 hours at 110 ℃ to remove the solvent. The final electrode material mass was 1 ± 0.1 mg/cm$^2$. Using half-cell system with 1 M LiOH electrolyte, (materials pressed on Ni-foam, the working electrode), (Hg/HgO, the reference electrode), and (the counter electrode from Pt mesh) were used to evaluate the positive electrode materials' electrochemical performance including CV and GCD measurements were done range from 0 to 0.6 V and -1 to 0 V, respectively. The specific capacity (Qc) of the proposed electrodes was determined using GCD curves and the formula[35]:

$$Qc = \frac{I \times \Delta t}{m} \quad \text{(C/g)} \quad (1)$$

$$Cs = I \times \Delta t / m \times \Delta V \text{ (F/g)} \quad (2)$$

where (I) signifies the specific current, (Δt) indicates discharge time, (m) provides mass loading and ΔV refers potential window (V).

### *2.5. Constructing hybrid supercapacitor device*

The $ZnCo_2O_4$ Nc@3DGr nanocomposite and 3DGr were implemented as positive and negative electrodes in a hybrid supercapacitor (HSC) with a nylon separator 120 mm thick in 1 M LiOH. The charge balance ratio of the anode (Q-) and cathode (Q+) must be examined to produce improved electrochemical efficiency for the HSC full device. The charge efficiency (Q), specific capacitance (Cs), energy (E), and power (P) densities for the assembled HSC device were assessed by applying the given equations[36,37];

$$Q = C \times \Delta V \times m \quad (3)$$

$$\frac{m+}{m-} = \frac{C- \times \Delta V-}{C+ \times \Delta V+} \quad (4)$$

$$E_{cell} = \frac{Cs_{cell} \times \Delta V^2}{7.2} \text{ (Wh/kg)} \quad (5)$$

$$P_{cell} = \frac{E_{cell} \times 3600}{\Delta t} \text{ (W/kg)} \quad (6)$$

$\Delta V$ implies the cell voltage (V), and $m$ reflect the total mass loading for the HSC electrode (g).

## 3. Results and discussion

### *3.1. Material Characterization*

The crystalline phase characteristics of the MOF-derived $ZnCo_2O_4$ nanocubes, 3DGr, and $ZnCo_2O_4$ Nc@3DGr nanocomposite are confirmed by powder XRD, as depicted in Fig. 1.

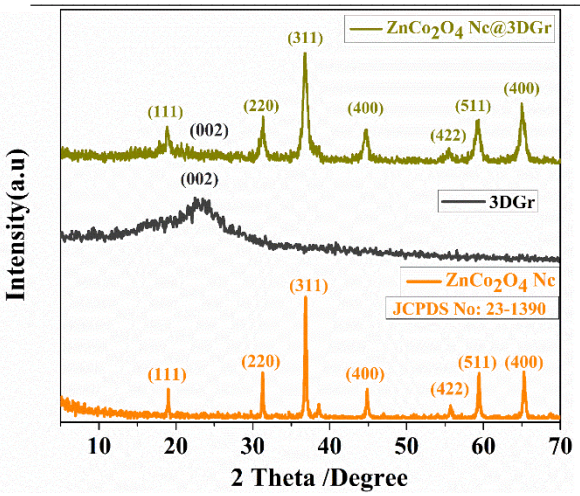


Fig. 1. XRD pattern for the fabricated materials-based hybrid supercapacitor electrodes.

The XRD pattern reveals seven distinct peaks corresponding to the cubic spinel bimetallic oxide structure. These peaks are detected at 2θ values of 19°, 31.1°, 36.8°, 44.5°, 55.5°, 59.2°, and 65.0°, and ascribed to the (111), (220), (311), (222), (400), (511), and (440) planes, respectively, of the pure $ZnCo_2O_4$ spinel phase (according to the JCPDS card No. 23–1390)[38,39]. No further peaks were seen in monoxides such as ZnO or $Co_3O_4$ phases, indicating the compound's phase purity. A prominent peak at an angle of 26.2º degrees may be assigned to the (002) plane of graphene, reflecting the absence of contaminants in the sample. The $ZnCo_2O_4$ Nc@3DGr hybrid composite exhibits the expected diffraction peaks of $ZnCo_2O_4$, which are seen with the broad characteristic peak of the 3DGr. The angles at which these peaks occur do not display any noticeable alteration. This finding provides evidence for the successful preparation of the composites intercalated between graphene layers in the fabricated $ZnCo_2O_4$ Nc@3DGr nanocomposite.

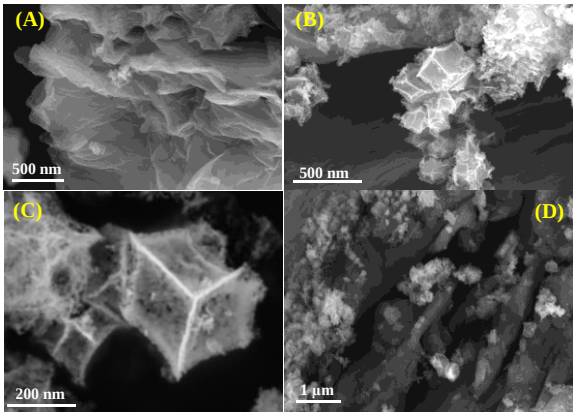


Fig. 2. FE-SEM images of the synthesized 3D graphene (a), $ZnCo_2O_4$ Nc (b), high magnification of $ZnCo_2O_4$ Nc (c), and $ZnCo_2O_4$ Nc@3DGr nanocomposite electrodes (d).

Fig. 2 depicts the FE-SEM images for the introduced electrode materials. As depicted in Fig 2 (a), the synthesized 3DGr sheets have a crumpled appearance reminiscent to silk structures, whereby they are intertwined with one another to form an interconnected three-dimensional network architecture. Interestingly, it is possible to generate a three-dimensional (3D) configuration using layers of graphene networks with a highly porous structure. This unique structure hinders the aggregation of graphene nanosheets and the subsequent restacking of layers upon the removal of functional groups. FE-SEM image in Fig. 2 (b) shows 3D nanocubes-like structure for the synthesized $ZnCo_2O_4$ which is attributed to the thermal decomposition of Zn-Co imidazole frameworks. The high magnification FE-SEM of the $ZnCo_2O_4$ Nc in Fig. 2 (c) reflected the ultra-porous structure with an average particle size of 275 nm due to the rearrangement of different metal source insertion into the organic framework after calcination. Fig. 2 (d) illustrates the intercalation of $ZnCo_2O_4$ Nc between graphene sheets creating a sandwich-like structure.

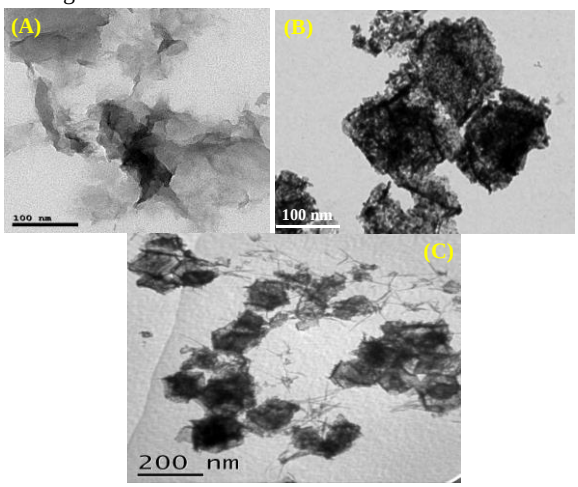


Fig. 3. TEM images of the synthesized 3D graphene (a), $ZnCo_2O_4$ Nc (b), and $ZnCo_2O_4$ Nc@3DGr nanocomposite electrodes.

TEM image in Fig. 3(a) reveals the existence of a 3D porous structure comprised of interconnected open-dead pores. The entire shape is encompassed by a graphene-based, overlapping net framework. The framework's three-dimensional structure is created by chemically coupling the functional groups of GO with triethylamine and followed by a lyophilizing procedure. TEM image in Fig. 3(b) further demonstrate numerous pores on the whole cubic surface reflecting a promising sacrificial template-based 3D nanocubes structure[40]. On the other hand, TEM image in Fig. 3 (c) provides that a 3D framework $ZnCo_2O_4$ Nc/3DGr nanocomposite is created when wrinkled graphene sheets are consistently wrapped around $ZnCo_2O_4$ nanocubes.

### *3.2. Electrochemical measurements for the synthesized electrode materials.*

To evaluate the storage capacity of the prepared electrodes, electrochemical measurements were carried out using a half-cell system with 3 electrodes. Fig. 4 (a) exhibits the CV profiles of the fabricated $ZnCo_2O_4$ Nc, $ZnCo_2O_4$ Nc@3DGr electrodes within a range (0.0 to 0.6V) of potential at (5 mV/s) scan rate. curve of $ZnCo_2O_4$ exhibits characteristic redox peaks that are associated with the reversible reaction occurring between the electrode material and the electrolyte. Nevertheless, incorporating graphene into $ZnCo_2O_4$ Nc@3DGr resulted in an enhanced peak current and a greater enclosed area, indicating an increase of redox reaction activity. This improvement may be due to the increased conductivity achieved by the integration of graphene. Furthermore, Fig. 4 (b) reveals that there is no visible collapse or modification in CV curves with increasing scan rates. This reflects a high-rate capability and remarkable reversibility. Fig. 4(c) displays the

GCD behaviour of the investigated electrodes at 1 A/g. The discharge time of the $ZnCo_2O_4$ Nc@3DGr electrode has a longer duration in comparison to that of the pure $ZnCo_2O_4$ Nc. The GCD profiles of the $ZnCo_2O_4$ Nc@3DGr were examined at various applied current densities, as seen in Fig. 4(d).

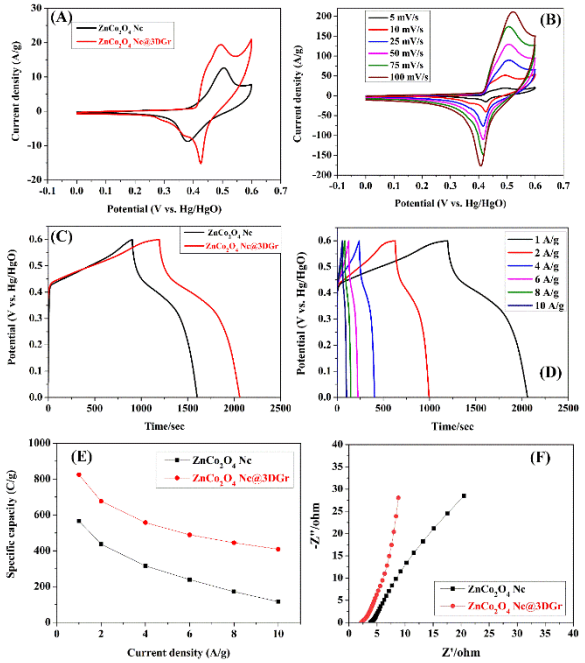


Fig. 4. Comparison CV curve at scan rate of 5 mV/s (a), CV profile for the $ZnCo_2O_4$ Nc@3DGr nanocomposite under various scan rates (b), GCD plot at 1A/g (c), GCD curves at different current densities for the $ZnCo_2O_4$ Nc@3DGr (d), specific capacity versus current densities (e) and Nyquist plot for the pure $ZnCo_2O_4$ Nc and $ZnCo_2O_4$ Nc@3DGr electrode (f)

The $ZnCo_2O_4$ Nc@3DGr material demonstrates the presence semi-triangular (GCD) profiles regardless exposed to greater current densities. The observed peaks in the GCD graph are indicative of the battery-like properties shown by the $ZnCo_2O_4$ Nc@3DGr electrode, which matches the results acquired from (CV) analysis. Fig. 4(e) reflects the estimated capacitances of the synthesized materials for various levels of current density according to the GCD curves. When GCD performed at 1 A/g, the $ZnCo_2O_4$ Nc@3DGr electrode achieved a substantially greater specific capacity (824.4 C/g, 1374 F/g), outperforming the pure $ZnCo_2O_4$ Nc electrode (567 C/g, 945 F/g). The $ZnCo_2O_4$ Nc@3DG electrode demonstrates the highest capacitance value due to the graphene layers effectively anchoring onto the cubic faces of the porous $ZnCo_2O_4$ Nc structure. This integration facilitates the rapid transfer of electrons by creating active sites and shortening the electron pathway. Additionally, it prevents aggregation of the graphene sheets, thereby enhancing the electrical conductivity of the nanocomposite[41].

In order to get a deeper understanding of the benefits associated with the electrodes, an analysis of the impedance was conducted for all samples that were generated. The Nyquist curves have been generated for the $ZnCo_2O_4$ and $ZnCo_2O_4$ Nc@3DGr Nc electrodes in the 0.01 Hz to 100000 Hz frequency range, as seen in Fig. 4(f). The $ZnCo_2O_4$ Nc@3DGr Nc exhibited a minimal crossing point with the real axis at high frequencies, implying a significantly reduced ohmic resistance (RS) of the electrolyte compared to the synthesized electrode materials. In relation to the sites of the intersection at high frequencies, it was observed that the internal resistances of the $ZnCo_2O_4$ Nc@3DGr Nc electrode exhibited a significant decrease (2.19 Ω) compared to the pristine $ZnCo_2O_4$ Nc (3.84 Ω), revealing an enhancement in electrical conductivity owing to incorporating of graphene in the nanocomposite. The electrode composed of $ZnCo_2O_4$ Nc@3DGr had the lowest levels of charge transfer, diffusive resistance, and a small semicircle diameter, indicating a low interfacial charge resistance (Rct) over a wide range of frequencies.

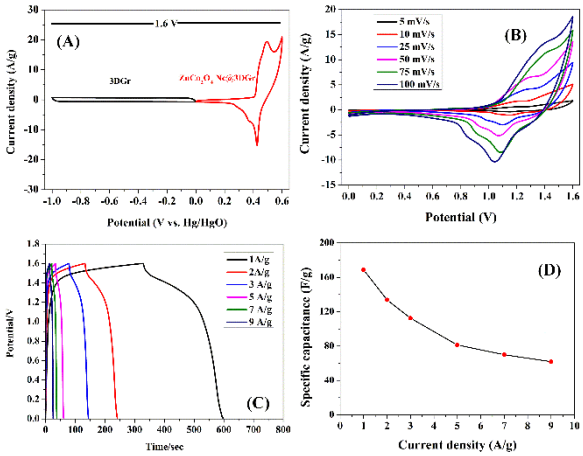


Fig. 5. CV curve at full potential windows of 3DGr and $ZnCo_2O_4$ Nc 5 mV/s (a), CV profile for the $ZnCo_2O_4$ Nc@3DGr //3DGr hybrid device under different sweep rates (b), GCD plot at current density from 1 A/g to 10 A/g (c), and specific capacitance versus current densities for the assembled $ZnCo_2O_4$ Nc@3DGr // 3DGr hybrid device (d).

To assess the effectiveness of electrode components in real supercapacitors technology, we employed a composite material of $ZnCo_2O_4$ Nc@3DGr (positive) and 3DGr (negative) electrode in order to construct the $ZnCo_2O_4$ Nc@3DGr // 3DGr HSC device. Fig. 5 (a) shows the 3DGr electrode's (CV) graph, which has a rectangular shape across the voltage of -1 to 0 V, reflecting ideal EDLC behaviour. The $ZnCo_2O_4$ Nc@3DGr electrode is employed in the right region of the CV profile with a voltage region from 0 to 0.6 V. As a result, a cell voltage of 1.6 V is acceptable for operation in a $ZnCo_2O_4$ Nc@3DGr //3DGr hybrid device. The results of a CV test performed at varied scan speeds (from 5 to 100 mV/s) are displayed in Fig. 5 (b). The examination of the CV test findings shows that the device's scan rate does not significantly change the form of the CV curve examined, demonstrating excellent rate and reversibility. As revealed in Fig. 5(c), the GCD curves provide a nearly symmetrical pattern when the current density is incremented from 1 to 10 A/g, signifying a substantial coulomb efficiency. According to Fig. 5(d), the specific capacitances of the HSC device were determined to be 168.75, 133.75, 112.5, 81.25, 70 and 61.87 F/g at current densities of 1, 2, 3, 5, 7, and 9 A/g, respectively.

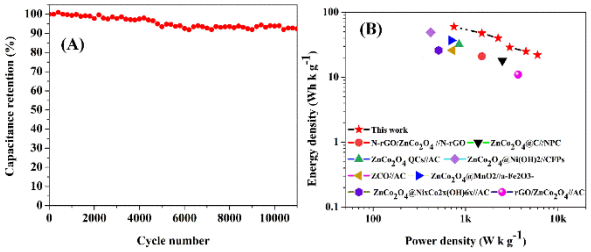


Fig. 6. Cycling stability performance for the constructed full HSC cell at 5 A/g (a), Ragone plot for the $ZnCo_2O_4$ Nc@3DGr // 3DGr HSC device comparison with other devices (b).

The considerable lifetime of the created HSC electrodes poses a significant obstacle to the development of commercialization efforts[42]. The recyclability assessment of the constructed $ZnCo_2O_4$ Nc@3DGr//3DGr HSC device was conducted by subjecting it to continuous charge/discharge cycles for over 11000 cycles at a rate of 5 A/g, as depicted in Fig. 6(a). After conducting a series of charge and discharge experiments for the purpose of stability testing, a total of 11,000 cycles were completed. The device has a retention rate of 93% in terms of its initial capacitance undergoing 11000 subsequent cycles. This finding suggests that the electrode materials used in the hybrid device were of ideal configuration design and outstanding chemical stability. Energy densities are frequently utilized as crucial parameters for evaluating the efficacy of fabricated $ZnCo_2O_4$ Nc@3DGr//3DGr device. According to the data presented in Fig. 6(b) of the Ragone plot, it can be observed that the HSCs exhibited an excellent energy density of 60 Wh/kg at a power consumption of 800 W/kg. Moreover, despite the rise of the maximum power density to 6000 W/kg, the resultant (HSC) device demonstrated a notable energy density of 22 Wh/kg, therefore exceeding the efficiency of previously reported HSC devices. Moreover, the electrochemical efficacy of the $ZnCo_2O_4$ Nc@3DGr HSC device in this work, as shown in the Ragone plot, is compared to the values reported in the references. The results indicate that the device shows greater energy and power densities than those documented in the literature[43–48].

## 4. Conclusions

In summary, three-dimensional graphene nanosheets and porous zinc cobaltite nanocubes were successfully fabricated based electrodes for enhanced hybrid supercapacitor devices. The $ZnCo_2O_4$ Nc@3DGr electrode delivered the capacity of 824.4 C/g compared to pristine 3D $ZnCo_2O_4$ Nc 567 C/g. Furthermore, the designed $ZnCo_2O_4$ Nc@3DGr // 3DGr hybrid supercapacitor device achieved a remarkable energy density of 60 Wh/kg and 800 W/kg of power density moreover ultra-long lifespan up to 11000 cycles with mentation capacitance retention of 93% from its initial capacitance. The exceptional electrochemical performance strongly implies that the optimal electro-active pathways play a significant role in ion and charge transport. The novelty of the $ZnCo_2O_4$ Nc@3DGr // 3DGr based hybrid supercapacitor device lies in its unique combination of holding the power and energy capabilities that address the demands of diverse energy storage applications in an innovative system. The distinguishing design of the fabricated $ZnCo_2O_4$ Nc@3DGr //3DGr-based hybrid supercapacitor device comes from its distinctive combination of robust power holding and energy capabilities, which effectively fulfils the requirements of various energy storage applications.

## 5. Acknowledgements

This paper is based upon work supported by Science, Technology & Innovation Funding Authority (STDF) under German-Egyptian Research Fund SUBLiME project (GERF-33649). This work contributes to the research performed at Beni-Suef University (Renewable Energy Science and engineering department)

## 6. Conflicts of interest

The authors declare that they have no known competing financial interests or personal relationships that could have appeared to influence the work reported in this paper.

## 7. References

[1] M. Salanne, B. Rotenberg, K. Naoi, K. Kaneko, P.L. Taberna, C.P. Grey, B. Dunn, P. Simon, Nat. Energy 1 (2016) 1–10.
[2] E. Karden, S. Ploumen, B. Fricke, T. Miller, K. Snyder, J. Power Sources 168 (2007) 2–11.
[3] S. Karthikeyan, B. Narenthiran, A. Sivanantham, L.D. Bhatlu, T. Maridurai, Mater. Today Proc. 46 (2021) 3984–3988.
[4] W. Raza, F. Ali, N. Raza, Y. Luo, K.-H. Kim, J. Yang, S. Kumar, A. Mehmood, E.E. Kwon, Nano Energy 52 (2018) 441–473.
[5] Poonam, K. Sharma, A. Arora, S.K. Tripathi, J. Energy Storage 21 (2019) 801–825.
[6] A. Muzaffar, M.B. Ahamed, K. Deshmukh, J. Thirumalai, Renew. Sustain. Energy Rev. 101 (2019) 123–145.
[7] M. Ibrahim, H.N. Abdelhamid, A.M. Abuelftooh, S.G. Mohamed, Z. Wen, X. Sun, J. Energy Storage 55 (2022) 105375.
[8] Y. Zhu, P. Lu, F. Li, Y. Ding, Y. Chen, ACS Appl. Energy Mater. 4 (2021) 3962–3974.
[9] Q. Liu, X. Hong, X. You, X. Zhang, X. Zhao, X. Chen, M. Ye, X. Liu, Energy Storage Mater. 24 (2020) 541–549.
[10] D.P. Chatterjee, A.K. Nandi, J. Mater. Chem. A 9 (2021) 15880–15918.
[11] W. Jiang, F. Hu, Q. Yan, X. Wu, Inorg. Chem. Front. 4 (2017) 1642–1648.
[12] J. Cherusseri, D. Pandey, J. Thomas, Batter. Supercaps 3 (2020) 860–875.
[13] G. Zhang, X. Xiao, B. Li, P. Gu, H. Xue, H. Pang, J. Mater. Chem. A 5 (2017) 8155–8186.
[14] M.A.A. Mohd Abdah, N.H.N. Azman, S. Kulandaivalu, Y. Sulaiman, Mater. Des. 186 (2020) 108199.
[15] H. Abdel-Gawad, R.M. Abdelhameed, Egypt. J. Chem. 64 (2021) 1257–1271.
[16] S. Wu, J. Liu, H. Wang, H. Yan, Int. J. Energy Res. 43 (2019) 697–716.
[17] H. Wang, Q.L. Zhu, R. Zou, Q. Xu, Chem 2 (2017) 52–80.
[18] M. El-Shahat, R.M. Abdelhameed, Appl. Catal. A Gen. 635 (2022) 118558.
[19] M.Y. Masoomi, A. Morsali, A. Dhakshinamoorthy, H. Garcia, Angew. Chemie 131 (2019) 15330–15347.
[20] A.D. Salunkhe, P.S. Pawar, P.K. Pagare, A.N. Kadam, P.K. Katkar, A.P. Torane, J. Electroanal. Chem. 939 (2023) 117475.
[21] H.S. Jadhav, A. Roy, W.J. Chung, J.G. Seo, Electrochim. Acta 246 (2017) 941–950.

[22] A.M. Khedr, S.Y. Attia, K. Shoueir, M.H. Misbah, H. El-Hosainy, S.G. Mohamed, M. El-Kemary, J. Alloys Compd. 968 (2023) 172280.
[23] G. Dhakal, D. Mohapatra, T.L. Tamang, M. Lee, Y.R. Lee, J.J. Shim, Energy 218 (2021) 119436.
[24] F. Su, Z.S. Wu, J. Energy Chem. 53 (2020) 354–357.
[25] Z. Wu, X. Yang, H. Gao, H. Shen, H. Wu, X. Xia, X. Wu, W. Lei, J. Yang, Q. Hao, J. Alloys Compd. 891 (2022) 162053.
[26] B. Naresh, C. Kuchi, S.K. Kummara, O.R. Ankinapalli, P.S. Reddy, Synth. Met. 293 (2023) 117283.
[27] H. Sun, Y. Miao, G. Wang, X. Ren, E. Bao, X. Han, Y. Wang, X. Ma, C. Xu, H. Chen, J. Energy Storage 72 (2023) 108502.
[28] P. Sivakumar, L. Kulandaivel, J. Park, C.J. Raj, R. Manikandan, H. Jung, J. Alloys Compd. 952 (2023) 170042.
[29] J. Bhagwan, S. Khaja Hussain, J.S. Yu, J. Alloys Compd. 815 (2020) 152456.
[30] L. Xu, Y. Zhao, J. Lian, Y. Xu, J. Bao, J. Qiu, L. Xu, H. Xu, M. Hua, H. Li, Energy 123 (2017) 296–304.
[31] J.A. Rajesh, B.-K. Min, J.-H. Kim, S.-H. Kang, H. Kim, K.-S. Ahn, J. Electroanal. Chem. 785 (2017) 48–57.
[32] Y. Shang, T. Xie, Y. Gai, L. Su, L. Gong, H. Lv, F. Dong, Electrochim. Acta 253 (2017) 281–290.
[33] X. Chen, N. Xin, Y. Li, C. Sun, L. Li, Y. Ying, W. Shi, Y. Liu, J. Mater. Sci. Technol. 127 (2022) 236–244.
[34] D.C. Marcano, D. V. Kosynkin, J.M. Berlin, A. Sinitskii, Z. Sun, A. Slesarev, L.B. Alemany, W. Lu, J.M. Tour, ACS Nano 4 (2010) 4806–4814.
[35] H. Jiang, L. Yang, C. Li, C. Yan, P.S. Lee, J. Ma, Energy Environ. Sci. 4 (2011) 1813–1819.
[36] M.A. Nassar, S.I. El-dek, W.M.A.E. Rouby, A.G. El-Deen, J. Energy Storage 44 (2021) 103305.
[37] S.A. Salheen, H.F. Nassar, S. Dsoke, A.G. El-Deen, Colloids Surfaces A Physicochem. Eng. Asp. 660 (2023) 130821.
[38] Y. Sharma, N. Sharma, G.V. Subba Rao, B.V.R. Chowdari, Adv. Funct. Mater. 17 (2007) 2855–2861.
[39] X. Song, Q. Ru, B. Zhang, S. Hu, B. An, J. Alloys Compd. 585 (2014) 518–522.
[40] A.G. El-Deen, M.K. Abdel-Sattar, N.K. Allam, Appl. Surf. Sci. 587 (2022) 152548.
[41] D. Nandi, V.B. Mohan, A.K. Bhowmick, D. Bhattacharyya, J. Mater. Sci. 55 (2020) 6375–6400.
[42] D.-G. Wang, Z. Liang, S. Gao, C. Qu, R. Zou, Coord. Chem. Rev. 404 (2020) 213093.
[43] G. Vignesh, R. Ranjithkumar, P. Devendran, N. Nallamuthu, S. Sudhahar, M. Krishna Kumar, Mater. Sci. Eng. B 290 (2023) 116328.
[44] J.M. Gonçalves, M.I. Da Silva, M.N.T. Silva, P.R. Martins, E. Nossol, H.E. Toma, L. Angnes, Energy Adv. (2022) 793–841.
[45] Y. Pan, H. Gao, M. Zhang, L. Li, G. Wang, X. Shan, J. Colloid Interface Sci. 497 (2017) 50–56.
[46] C. Du, E. Han, L. Sun, S. Qiao, L. Li, Ionics (Kiel). 26 (2020) 383–391.
[47] W. Ma, H. Nan, Z. Gu, B. Geng, X. Zhang, J. Mater. Chem. A 3 (2015) 5442–5448.
[48] Z. Gao, L. Zhang, J. Chang, Z. Wang, D. Wu, F. Xu, Y. Guo, K. Jiang, Appl. Surf. Sci. 442 (2018) 138–147.